

Fast and Shadow Region 3-Dimensional Imaging Algorithm With Range Derivative of Doubly Scattered Signals for UWB Radars

Shouhei Kidera, *Member, IEEE*, and Tetsuo Kirimoto, *Senior Member, IEEE*

Abstract—Ultra-wideband (UWB) radar with its high range resolution and applicability to optically harsh environments, offer great promise for near field sensing systems. It is particularly suitable for robotic or security sensors that must identify a target in low visibility. Some recently developed radar imaging algorithms proactively employ multiple scattered components, which can enhance an imaging range compared to synthesizing a single scattered component. We have already proposed the synthetic aperture radar (SAR) method considering a double scattered, which successfully expanded a reconstructible range of radar imagery with no *a priori* knowledge of target or surroundings. However, it requires a multiple integration of the received signals, requiring the fifth times integration in the 3-D case. Thus, this method requires an intensive computation and its spatial resolution is insufficient for clear boundary extraction such as edges or specular surfaces. As a substantial solution, this paper proposes a novel shadow region imaging algorithm based on a range derivative of double scattered signals. This new method accomplishes high-speed imaging, including a shadow region without any integration process, and enhances the accuracy with respect to clear boundary extraction. Results from numerical simulations verify that the proposed method remarkably decreases the computation amount compared to that for the conventional method, especially for the 3-D problem, enhancing the visible range of radar imagery.

Index Terms—Fast and shadow region imaging, multiple scattered wave, range derivative of double scattered signal, range points migration, ultra-wideband (UWB) radar.

I. INTRODUCTION

Ultra-wideband (UWB) pulse radar with high range resolution fulfills its potential for near-field sensing techniques. A robotic sensor is one of the most promising applications of UWB radar, able to identify a human body even in optically blurry visibilities, such as dark smog in disaster areas or high-density gas in resource exploration scenes. It is also

in demand for non-contact measurement in manufacturing reflector antennas or aircraft bodies requiring high-precision surfaces. Furthermore, it has a potential for accurate surface extraction of the human breast for detecting breast cancer, where the surface reflection from a breast often causes severe interference [1], [2]. While various radar imagery algorithms have been developed based on the aperture synthesis [3], the time reversal approach [4], [5], the range migration [6], [7] or genetic algorithm (GA)-based solutions for domain integral equations [8], they are not suitable for the above applications because it is, in general, difficult to achieve both low computation cost and high spatial resolution. To conquer the problem in the conventional techniques, we have already proposed a number of radar imaging algorithms, which accomplish real-time and high-resolution surface extraction beyond a pulse width [9], [10]. Although these algorithms have been applied to surface imaging, such as breast cancer detection [2], through-the-wall imaging [11], or human activity recognition [12], they are actually applicable only to simple shapes such as convex objects. As a high-speed and accurate 3-D imaging method feasible for complex-shaped targets, the range points migration (RPM) algorithm has been established [13]. This algorithm directly estimates an accurate direction of arrival (DOA) with the global characteristic of observed range points, avoiding the difficulty of connecting them. Although RPM is based on a simple idea, it offers accurate and super-resolution surface extraction by incorporating a frequency domain interferometer [14]. However, the above methods including [13] and [14] have the unresolvable problem that aperture size strictly constrains the imaging range of a target surface. In many cases, a major part of a target shape, such as a side of the target, falls into a shadow region, that is not reconstructed since only single scattered components are used for imaging.

To resolve this difficulty and enhance imaging range, the SAR algorithm considering a double scattered path has been developed [15]. Although this method shows that shadow region imaging is possible by positively using double scattered signals without preliminary observations or target models, which are required in other algorithms [16], [17], the method requires multiple integrations of the received signals. This incurs a large computation cost, especially for obtaining a full 3-D image. Moreover, the spatial resolution of SAR is often insufficient to identify target shapes particularly for edges or wedges owing to a range resolution limited by frequency bandwidth of UWB pulse, even if a large aperture size, i.e., high azimuthal resolution, is obtained.

Manuscript received December 09, 2010; revised May 31, 2011; accepted August 29, 2011. Date of publication October 21, 2011; date of current version February 03, 2012. This work was supported in part by the Grant-in-Aid for Scientific Research (B) (Grant 22360161), and the Grant-in-Aid for Young Scientists (Start-up) (Grant 21860036), promoted by the Japan Society for the Promotion of Science (JSPS).

The authors are with the Graduate School of Informatics and Engineering, University of Electro-Communications, Tokyo 182-8585, Japan (e-mail: kidera@ee.uec.ac.jp).

Color versions of one or more of the figures in this paper are available online at <http://ieeexplore.ieee.org>.

Digital Object Identifier 10.1109/TAP.2011.2173128

As an essential solution for these problems, this paper proposes a novel imaging algorithm based on the range derivative of doubly scattered signals, where an initial image obtained by RPM is used to the best effect. This method is based on an original proposition that each DOA of the double scattered points is strictly derived from the derivative of range points both in the 2-D and 3-D cases. This proposition enables us to directly estimate a target boundary corresponding to the doubly scattered centers without any integration procedures. The results of numerical simulations, investigating various target shapes and computational complexities, show that the proposed method accomplishes high-speed target boundary extraction in situations, which produce a shadow using existing techniques.

II. 2-D PROBLEM

A. System Model

Fig. 1 shows a system model for the 2-D model. It assumes a mono-static radar with an omnidirectional antenna scanning along the x -axis. A static target with an arbitrary shape is assumed, the spatial gradient of conductivity or permittivity on its boundary is expressed with Dirac's delta function [9], a so-called clear boundary. This assumption is generally acceptable for most indoor UWB sensors, for which omnidirectional radiation can be achieved by a small micro-strip antenna, as in [14], and the surroundings of sensors should be artificial objects such as furniture or walls with clear boundaries in terms of the center wavelength of a general UWB pulse. Due to the static object assumption, the scanning velocity is not relevant here. The propagation speed c of the radio wave is assumed to be a known constant. A transverse electric (TE) mode wave and cylindrical wave propagation is considered. A mono-cycle pulse is used as the transmitting current. The space in which the target and antenna are located is expressed by the parameters (x, z) . The parameters are normalized by λ , which is the central wavelength of the pulse. $z > 0$ is assumed for simplicity. $s'(X, t)$ is defined as the electric field received at antenna location $(x, z) = (X, 0)$ at time t . $\tilde{s}(X, t)$ is calculated by applying the Wiener filter to $s'(X, t)$ as

$$\tilde{s}(X, t) = \int_{-\infty}^{\infty} W(\omega) S'(\omega) e^{i\omega t} d\omega \quad (1)$$

where $S'(X, \omega)$ is the signal in the frequency domain of $s'(X, t)$. $W(\omega)$ is defined as

$$W(\omega) = \frac{S_{\text{ref}}(\omega)^*}{(1 - \eta)S_0^2 + \eta|S_{\text{ref}}(\omega)|^2} S_0 \quad (2)$$

where $\eta = 1/(1+(S/N)^{-1})$, and $S_{\text{ref}}(\omega)$ is the reference signal in the frequency domain, which is the complex conjugate of that of the transmitted signal. S_0 is a constant for dimension consistency. This filter is an optimal mean square error (MSE) linear filter for additive noises. $\tilde{s}(X, t)$ is now converted to $s(X, Z)$ using the valuable conversion $Z = ct/2\lambda$ where c is the speed of the radio wave.

B. Conventional Imaging Algorithms

Two methods are introduced as the conventional imaging algorithms for comparison with the proposed method. One

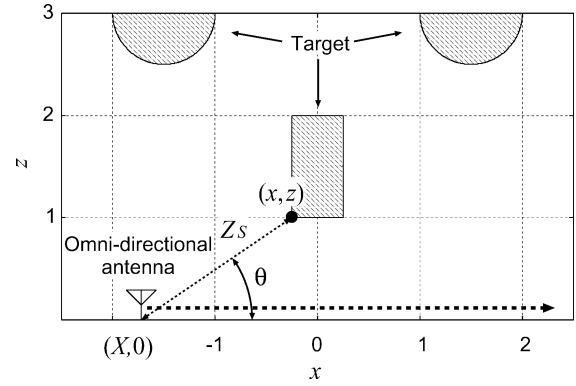


Fig. 1. System model in the 2-D problem.

is RPM, which achieves accurate high-speed target imaging even with a complex-shaped boundary, and employs a single scattered wave [13], [14]. The second is SAR extended for double scattered waves [15].

1) *RPM*: As one of the most promising imaging algorithms applicable to various target shapes, the RPM algorithm has been established. First, this method extracts the group of range points as (X, Z_S) , which satisfy the local maxima of $s(X, Z)$. Basically, RPM assumes that a target boundary point (x, z) exists on a circle with center $(X, 0)$ and radius Z_S , following from the assumption of an omnidirectional antenna and cylindrical propagation of a TE mode wave, and employs an accurate DOA (θ in Fig. 1) estimation by making use of the global characteristics of the observed range map. The optimum θ_{opt} is calculated as

$$\theta_{\text{opt}}(\mathbf{q}) = \arg \max_{0 \leq \theta \leq \pi} \left| \sum_{i=1}^{N_R} s(\mathbf{q}_i) e^{-\left\{ \frac{(X-X_i)^2}{2\sigma_X^2} + \frac{(\theta - \theta(\mathbf{q}, \mathbf{q}_i))^2}{2\sigma_\theta^2} \right\}} \right| \quad (3)$$

where $\mathbf{q} = (X, Z_S)$, $\mathbf{q}_i = (X_i, Z_{S,i})$, and N_R is the number of the range points. $\theta(\mathbf{q}, \mathbf{q}_i)$ denotes the angle from the x axis to the intersection point of the circles, with parameters (X, Z_S) and $(X_i, Z_{S,i})$. The target boundary (x, z) for each range point (X, Z_S) is expressed as $x = X + Z_S \cos \theta_{\text{opt}}(\mathbf{q})$ and $z = Z_S \sin \theta_{\text{opt}}(\mathbf{q})$. This algorithm ignores range points connection, and produces accurate target points, even if an extremely complicated range distribution is given. It also has the significant advantage that each target point (x, z) and range point (X, Z_S) satisfies a one-to-one correspondence, which takes a substantial role in the proposed method described in the following section.

The performance example of RPM is presented here, where the received electric field is calculated by the finite-difference time-domain (FDTD) method. The range points (X, Z_S) are extracted from the local peaks of $s(X, Z')$ which are beyond the preliminary determined threshold [13]. An example of this method for the target shape shown in Fig. 1 is presented. Fig. 2 shows the output of the Wiener filter, and the extracted range points as (X, Z_S) . The received signals are calculated at 401 locations for $-2.5 \leq X \leq 2.5$. A noiseless environment is assumed. The positive local maxima are regarded as the range points originated from the single scattered waves and, on the contrary, the negative ones are regarded as the range points originated from the double scattered components, because they have, in general, an anti-phase relationship. Fig. 3 shows the estimated target points obtained by RPM. $\sigma_X = 1.0\lambda$ and

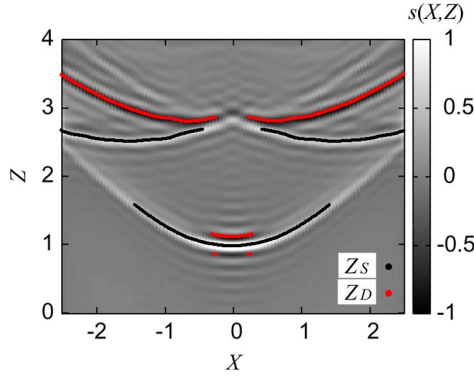


Fig. 2. Output of Wiener filter $s(X, Z)$ for the multiple targets and range points as (X, Z_S) and (X, Z_D) .

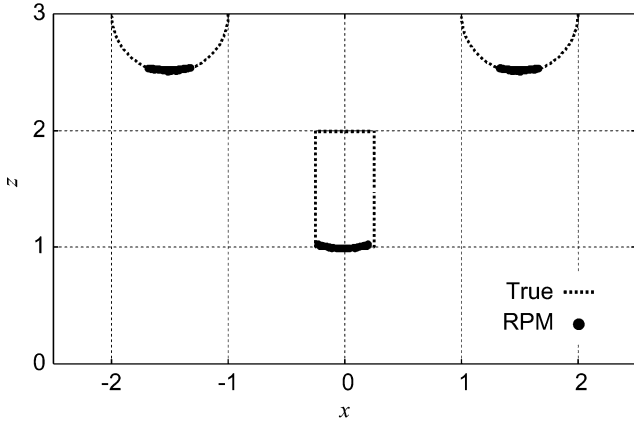


Fig. 3. Estimated image with RPM for the multiple targets.

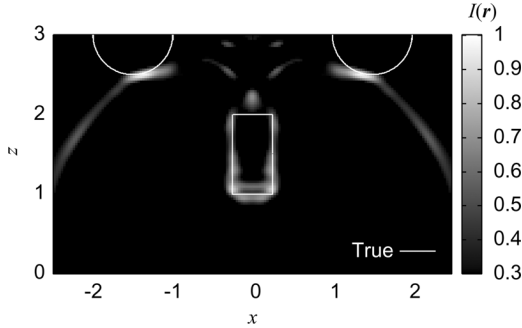


Fig. 4. Estimated image with the SAR $I(\mathbf{r})$ using double scattered signals for the multiple targets.

$\sigma_\theta = \pi/50$ are empirically determined by considering robustness and accuracy for imaging, as detailed in [13]. This figure indicates that the target points accurately express the front side of the target boundary, but the rectangular side of the boundary mostly falls into a shadow region. This is because each antenna receives a distinguishable echo from the target boundary, which is perpendicular to the direction of the line of sight from each antenna location. This is an inherent problem in all algorithms that use only a single scattered wave for target reconstruction.

2) *SAR With Double Scattered Signals*: SAR employing the double scattered signal has been developed to enhance the imaging range, including a shadow [15]. Here, the same system and signal models are used as in Section II-A. In general, a double scattered wave propagates with a different path from that of a single scattered one. It, therefore, often provides independent information as to the two scattering points. This

method calculates the image using double scattered waves as $I_2(\mathbf{r})$

$$I_2(\mathbf{r}) = - \int_{\mathbf{r}' \in R} \int_{X \in \Gamma} I_1(\mathbf{r}') s(X, d_2(\mathbf{r}, \mathbf{r}', X)/2) dX d\mathbf{r}' \quad (4)$$

where $\mathbf{r}' = (x', z')$, R denotes the region of real space, $s(X, *)$ is the output of the Wiener filter, and $d_2(\mathbf{r}, \mathbf{r}', X) = \sqrt{(x-X)^2 + z^2} + \sqrt{(x'-X)^2 + z'^2} + \sqrt{(x-x')^2 + (z-z')^2}$. The minus sign in (4) creates a positive image focused by double scattered waves that have an antiphase relationship from a single scattered one. Here, the initial image $I_1(\mathbf{r})$ is defined as the original SAR image as

$$I_1(\mathbf{r}) = \int_{X \in \Gamma} s(X, d_2(\mathbf{r}, \mathbf{r}, X)/2) dX. \quad (5)$$

Equation (4), simple expression of the aperture synthesis of the received signals by considering a double scattered path, can be regarded as a coherent integration scheme because $I_1(\mathbf{r})$ denotes the amplitude and its positive outputs offer the target boundary. Any extension of the SAR algorithm, such as omega-k migration [18] range-Doppler, can be used in creating $I_1(\mathbf{r})$. The final image is defined as

$$I'(\mathbf{r}) = \frac{I_1(\mathbf{r})H(I_1(\mathbf{r}))}{\max_{\mathbf{r}} I_1(\mathbf{r})} + \frac{I_2(\mathbf{r})H(I_2(\mathbf{r}))}{\max_{\mathbf{r}} I_2(\mathbf{r})} \quad (6)$$

where $H(*)$ is the Heaviside function.

The performance evaluation of this method is shown as follows. Fig. 4 shows the estimated image $I(\mathbf{r})$ for the previous target case, using the same data as in Fig. 2. $I(\mathbf{r})$ is normalized by its maximum value. Fig. 4 shows that the part of the side region of the rectangular target can be reproduced, and that the visible ranges of the circle and rectangular boundaries are remarkably expanded. The reason is that double scattered waves are effectively focused on the part of the target side in (4). It also claims that this method does not require target modeling or *a priori* information of the surroundings.

However, it requires a triple integration for imaging and its calculation time goes up to around 60 s for Intel Pentium D 2.8-GHz processor. In the 3-D case, such a large calculation burden becomes more severe for a robotic sensor because it basically requires a fifth times integration for each image frame. Moreover, some false images occur around the target boundary, due to the range sidelobe of filter responses or other components like triple scattering ones; it also offers a blurry boundary, where its spatial resolution is strictly limited by half of a pulse width.

C. Proposed Method

To overcome the problems described for conventional methods, this paper proposes an accurate high-speed imaging algorithm for the shadow region. This method employs target points, which are preliminarily created by RPM, and directly reconstructs the target points corresponding to the double scattered signals, where each derivative of the range points is employed.

1) *Principle of Proposed Method*: This subsection describes a basic theory of the proposed method, indicating the relationship between the range points and the doubly scattered centers. Here, two target points originating from the doubly scat-

tering are defined as $\mathbf{p}_1 = (x_1, z_1)$ and $\mathbf{p}_2 = (x_2, z_2)$, respectively. As previously described, a double scattered signal has an anti-phase relationship to a single scattered one [15]; the negative peaks of $s(X, Z)$ are mostly regarded as double scattered echoes. Then, (X, Z_D) is defined as the range point of a double scattered wave, which is extracted from the local minimum of $s(X, Z)$. $\mathbf{p}_L = (X, 0)$ denotes an antenna location. In this case, the following proposition holds.

Proposition 1: When $\partial Z_D / \partial X$ exists on (X, Z_D) , the next relationship holds:

$$\frac{\partial Z_D}{\partial X} = -\frac{\cos \theta_1 + \cos \theta_2}{2} \quad (7)$$

where $\theta_1 = \cos^{-1}((x_1 - X)/(Z_1))$, $\theta_2 = \cos^{-1}((x_2 - X)/(Z_2))$, $Z_1 = \|\mathbf{p}_1 - \mathbf{p}_L\|$, and $Z_2 = \|\mathbf{p}_2 - \mathbf{p}_L\|$ are defined, and $0 \leq \theta_1, \theta_2 \leq \pi$ hold. This method assumes that a double scattered path satisfies the law of reflection on each scattering boundary; that is regarded as a phase stationary condition.

The proof of this proposition is described in Appendix A. It is naturally derived as $|\partial Z_D / \partial X| \leq 1$, which is used for the actual procedure of the proposed method, as described in the following section. If $\mathbf{p}_1 = \mathbf{p}_2$ holds, regarded as single scattered case, (7) is equivalent to inverse boundary scattered transform (IBST) in [9]. Here, \mathbf{p}_2 is expressed as

$$\mathbf{p}_2 = \mathbf{p}_L + (Z_2 \cos \theta_2, Z_2 \sin \theta_2) \quad (8)$$

Once a first scattering point \mathbf{p}_1 is determined, θ_2 is given as

$$\theta_2 = \cos^{-1}(-2\partial Z_D / \partial X - \cos \theta_1). \quad (9)$$

In addition, if the normal vector as \mathbf{e}_n on \mathbf{p}_1 is given, the law of reflection derives Z_2 as

$$Z_2 = \frac{1}{2} \frac{Z_1^2 + (2Z_D - Z_1)^2 + 2(2Z_D - Z_1)(\mathbf{p}_1 - \mathbf{p}_L) \cdot \mathbf{e}_3}{(\mathbf{p}_1 - \mathbf{p}_L) \cdot \mathbf{e}_3 + 2Z_D - Z_1} \quad (10)$$

where

$$\mathbf{e}_3 = \mathbf{e}_1 - 2(\mathbf{e}_n \cdot \mathbf{e}_1)\mathbf{e}_n \quad (11)$$

holds with $\mathbf{e}_1 = (\mathbf{p}_1 - \mathbf{p}_L) / \|\mathbf{p}_1 - \mathbf{p}_L\|$. The derivation of (10) is described in Appendix B. \mathbf{p}_2 obviously satisfies the following condition as

$$\mathbf{p}_2 = \mathbf{p}_1 + Z_3 \mathbf{e}_3 \quad (12)$$

where $Z_3 = \|\mathbf{p}_2 - \mathbf{p}_1\|$ holds. Fig. 5 shows the relationship among the scattered points \mathbf{p}_1 , \mathbf{p}_2 and the antenna location \mathbf{p}_L .

2) *Incorporation With RPM:* A substantial idea of the proposed method is that it makes uses of the preliminary estimated target points by RPM as the first scattering location \mathbf{p}_1 with its normal vector \mathbf{e}_n . As previously described in Section II-B1, RPM directly converts the range points to the target points, satisfying a one-to-one correspondence. Here we define each target point and range point with RPM as $\mathbf{p}_i^{\text{rpm}} \equiv (x_i^{\text{rpm}}, z_i^{\text{rpm}})$ and $\mathbf{q}_i^{\text{rpm}} \equiv (X_i^{\text{rpm}}, Z_i^{\text{rpm}})$, ($i = 1, \dots, N_T^{\text{rpm}}$), where N_T^{rpm} is the

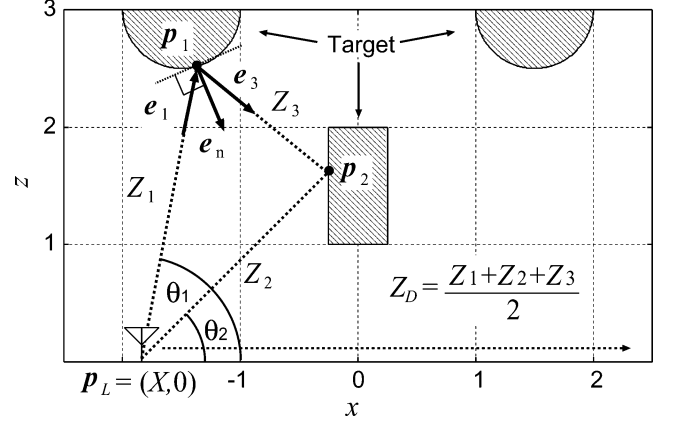


Fig. 5. Relationship among the double scattered points \mathbf{p}_1 , \mathbf{p}_2 , and the antenna location \mathbf{p}_L .

total number of target points by RPM. In addition, each normal vector $\mathbf{e}_{n,i}^{\text{rpm}}$ on $\mathbf{p}_i^{\text{rpm}}$ is given by

$$\mathbf{e}_{n,i}^{\text{rpm}} = \frac{(X_i^{\text{rpm}} - x_i^{\text{rpm}}, -z_i^{\text{rpm}})}{Z_i^{\text{rpm}}}. \quad (13)$$

This relationship is derived from the assumption that each antenna receives a strong echo from the target boundary, which is perpendicular to a direction for a line of sight [13]. Equation (13) indicates that the inclination of the target boundary is directly estimated without using derivative operations; it is applicable even for a non-differentiable point like an edge. In addition, target points obtained by RPM on edges are reconstructed from different antenna locations, because an edge diffraction wave can be received in a wider observation range. Such points have different normal vectors, which are directly related to \mathbf{e}_3 , and contribute to the search for a secondary scattering center first diffracted from an edge.

This algorithm determines an optimal \mathbf{p}_1 from a set of target points obtained by RPM, which is defined as $\mathcal{T}_{\text{rpm}} = \{(x, z) \in \bigcup_{i=1}^{N_T^{\text{rpm}}} \mathbf{p}_i^{\text{rpm}}\}$. Here, the parameter vector \mathbf{P}_i , ($i = 1, \dots, N_T^{\text{rpm}}$) is also defined as

$$\mathbf{P}_i \equiv (\mathbf{R}_i^{\text{rpm}}, \mathbf{Q}_D) \quad (14)$$

$$\mathbf{Q}_D \equiv (\mathbf{p}_L, Z_D, \partial Z_D / \partial X) \quad (15)$$

$$\mathbf{R}_i^{\text{rpm}} \equiv (\mathbf{p}_i^{\text{rpm}}, \mathbf{q}_i^{\text{rpm}}, \mathbf{e}_{n,i}^{\text{rpm}}, \mathbf{e}_{1,i}^{\text{rpm}}, \mathbf{e}_{3,i}^{\text{rpm}}) \quad (16)$$

where $\mathbf{e}_{1,i}^{\text{rpm}} = (\mathbf{p}_i^{\text{rpm}} - \mathbf{p}_L) / \|\mathbf{p}_i^{\text{rpm}} - \mathbf{p}_L\|$, and $\mathbf{e}_{3,i}^{\text{rpm}}$ is determined in (11), similarly. To select the optimal \mathbf{p}_1 from \mathcal{T}_{rpm} , two conditions for \mathbf{p}_2 are introduced as follows. First, using (8), $\mathbf{p}_2^A(\mathbf{P}_i)$ is defined as

$$\mathbf{p}_2^A(\mathbf{P}_i) \equiv \mathbf{p}_L + (Z_2(\mathbf{P}_i) \cos \theta_2(\mathbf{P}_i), Z_2(\mathbf{P}_i) \sin \theta_2(\mathbf{P}_i)) \quad (17)$$

where $Z_2(\mathbf{P}_i)$ and $\theta_2(\mathbf{P}_i)$ are calculated in (10) and (9), respectively. Second, considering another condition in (12), $\mathbf{p}_2^B(\mathbf{P}_i)$ is defined as

$$\mathbf{p}_2^B(\mathbf{P}_i) \equiv \mathbf{p}_i^{\text{rpm}} + Z_3(\mathbf{P}_i) \mathbf{e}_{3,i}^{\text{rpm}} \quad (18)$$

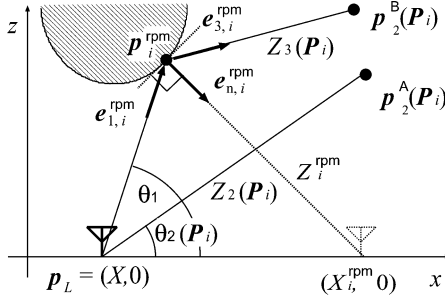


Fig. 6. Relationship between \mathbf{p}_2^A and \mathbf{p}_2^B as two candidates for \mathbf{p}_2 .

where $Z_3(\mathbf{P}_i) = 2Z_D - Z_2(\mathbf{P}_i) - \|\mathbf{p}_i^{\text{rpm}} - \mathbf{p}_L\|$. Fig. 6 shows the relationship between two candidates for \mathbf{p}_2 as $\mathbf{p}_2^A(\mathbf{P}_i)$ and $\mathbf{p}_2^B(\mathbf{P}_i)$. Then, the proposed method determines the optimum candidate $\hat{\mathbf{p}}_1$ for each \mathbf{Q}_D as

$$\hat{\mathbf{p}}_1(\mathbf{Q}_D) = \underset{\mathbf{p}_i^{\text{rpm}} \in \mathcal{T}_{\text{RPM}}}{\text{argmin}} \|\mathbf{p}_2^A(\mathbf{P}_i) - \mathbf{p}_2^B(\mathbf{P}_i)\|^2. \quad (19)$$

The optimum second scattering point $\hat{\mathbf{p}}_2(\mathbf{Q}_D)$ is determined as

$$\hat{\mathbf{p}}_2(\mathbf{Q}_D) = \frac{\mathbf{p}_2^A(\hat{\mathbf{P}}) + \mathbf{p}_2^B(\hat{\mathbf{P}})}{2} \quad (20)$$

where $\hat{\mathbf{P}}$ is defined as \mathbf{P}_i , when the evaluation value in the right term in (19) becomes minimum. This optimization scheme is based on the assumption that if $\hat{\mathbf{p}}_2(\mathbf{Q}_D)$ is the actual target point, it must satisfy both (8) and (12). Note that this method does not employ an integration of the scattered signals but directly determines the double scattering points using the derivative of the range points.

Furthermore, a false image reduction scheme is introduced. In the postprocessing, $\hat{\mathbf{p}}_2(\mathbf{Q}_D)$ is regarded as a false image, if the following condition is satisfied:

$$\zeta(\hat{\mathbf{p}}_2(\mathbf{Q}_D)) \geq \gamma \quad (21)$$

where γ is an empirically determined threshold, and $\zeta(\hat{\mathbf{p}}_2(\mathbf{Q}_D))$ is defined as

$$\zeta(\hat{\mathbf{p}}_2(\mathbf{Q}_D)) = \sum_{i=1}^{N_T^{\text{rpm}}} \exp \left\{ -\frac{D(\mathbf{p}_i^{\text{rpm}}, \hat{\mathbf{p}}_2(\mathbf{Q}_D), \mathbf{p}_L)^2}{2\sigma_F^2} \right\} \times \exp \left\{ -\frac{\|\hat{\mathbf{p}}_2(\mathbf{Q}_D) - \mathbf{p}_L\|^2}{2(Z_i^{\text{rpm}}/2)^2} \right\} \quad (22)$$

where $D(\mathbf{p}_i^{\text{rpm}}, \hat{\mathbf{p}}_2(\mathbf{Q}_D), \mathbf{p}_L) = \|\mathbf{p}_i^{\text{rpm}} - \hat{\mathbf{p}}_2(\mathbf{Q}_D)\| + \|\hat{\mathbf{p}}_2(\mathbf{Q}_D) - \mathbf{p}_L\| - \|\mathbf{p}_i^{\text{rpm}} - \mathbf{p}_L\|$ and $\sigma_F = 0.5\lambda$. $\zeta(\hat{\mathbf{p}}_2(\mathbf{Q}_D))$ increases when the following two conditions are satisfied. First, a large number of the first Fresnel zones determined by target points with RPM, regarded as \mathbf{p}_1 , include the double scattering point as $\hat{\mathbf{p}}_2(\mathbf{Q}_D)$. Second, $\hat{\mathbf{p}}_2(\mathbf{Q}_D)$ exists close to the antenna location compared to the observed range of single scattering Z_i^{rpm} . We assume that both situations are inadmissible for the actual target points. The similar scheme for a false image reduction is described in [15].

3) *Procedure of the Proposed Algorithm:* The actual procedure of the proposed method is summarized as follows.

Step 1) A set of target points \mathcal{T}_{RPM} is obtained by RPM.

Step 2) Range points are extracted as $(X_j, Z_{D,j})$, ($j = 1, \dots, N_D$) from the output of a Wiener filter, according to the condition given as

$$\left. \begin{aligned} \partial s(X, Z)/\partial Z &= 0 \\ s(X, Z) &\leq \beta \min_Z s(X, Z) \end{aligned} \right\} \quad (23)$$

where N_D is the total number of range points of the double scattered signals, and β is empirically determined.

Step 3) For each $(X_j, Z_{D,j})$, $\partial Z_{D,j}/\partial X$ is calculated by the difference approximation with Gaussian weighting as

$$\frac{\partial Z_{D,j}}{\partial X} = \frac{\sum_{k=1}^{N'_D} \frac{Z_{D,j} - Z_{D,k}}{X_j - X_k} \exp \left\{ -\frac{(X_j - X_k)^2}{2\sigma_{\text{DX}}^2} \right\}}{\sum_{k=1}^{N'_D} \exp \left\{ -\frac{(X_j - X_k)^2}{2\sigma_{\text{DX}}^2} \right\}} \quad (24)$$

where σ_{DX} is empirically determined and N'_D denotes the number of range points of $(X_k, Z_{D,k})$, which satisfy $|(Z_{D,j} - Z_{D,k})/(X_j - X_k)| \leq 1$. The parameter $\mathbf{Q}_{D,j}$ is created in (15) is stored into a set as $\mathcal{Q}_D = \{(X, 0, Z_D, \partial Z_D/\partial X) \in \bigcup_{j=1}^{N_D} \mathbf{Q}_{D,j}\}$.

Step 4) For each $\mathbf{Q}_{D,j}$ from \mathcal{Q}_D , $\mathbf{R}_i^{\text{rpm}}$ is created in (16). Then, $\hat{\mathbf{p}}_1(\mathbf{Q}_{D,j})$ and $\hat{\mathbf{p}}_2(\mathbf{Q}_{D,j})$ are determined in (19) and (20), respectively.

Step 5) If $\hat{\mathbf{p}}_2(\mathbf{Q}_{D,j})$ does not satisfy the condition in (21), it is added to the set of the target points \mathcal{T}_D .

Step 6) Steps 4) to 5) are iterated until \mathcal{Q}_D becomes empty.

Step 7) Obtain the final set of target points as $\mathcal{T} = \mathcal{T}_{\text{RPM}} \cup \mathcal{T}_D$.

Step 3) avoids the fatal sensitivity caused by the derivative operations by taking an appropriate value for σ_{DX} . Although this method needs an optimization procedure for \mathbf{p}_1 , it requires no integration process, directly locating the accurate target points.

D. Performance Evaluation Using Numerical Simulation

This section presents numerical examples performed by the proposed method for two target cases. Fig. 7 illustrates the target points reproduced by RPM and the proposed methods, where the true range points for single and double scattered signals are given by a geometrical optics approximation [15]. Here, $\sigma_{\text{DX}} = 0.3\lambda$, $\gamma = 100$, and $\beta = 0.3$ are set. This figure indicates that the proposed method accurately creates the target points around the side of the rectangular boundary. This verifies that if the actual range points are given, our method obtains extremely accurate boundary extraction, including shadow regions. As a realistic case, Fig. 8 presents the estimated target points with RPM and the proposed method, where the same data as in Fig. 2 are used. This figure exemplifies that this method produces many accurate target points around the rectangular side. Here, it should be noted that the RPM reconstructs the rectangular edge points as in Fig. 3, which are converted from the multiple range points (X, Z_S) on the part of the hyperbolic curve for which $|X| > 0.5\lambda$ and $1.0 \leq Z_S \leq 1.5$ in Fig. 2.

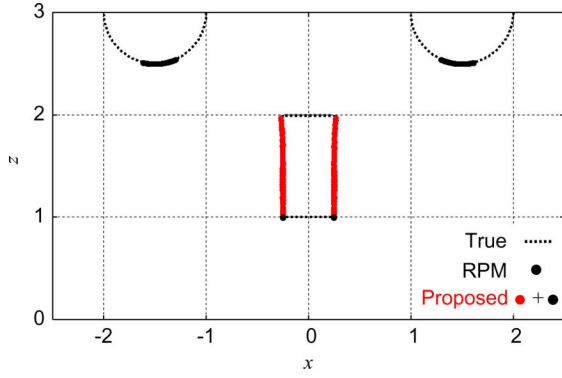


Fig. 7. Estimated image with RPM and the proposed method for the multiple objects, when true range points are given.

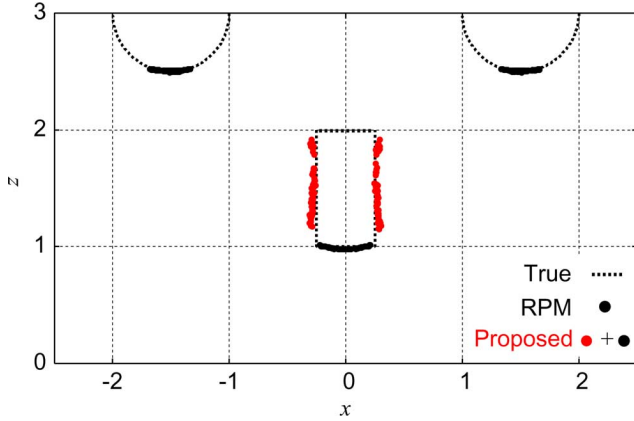


Fig. 8. Estimated image with RPM and the proposed method for the multiple objects, when range points are extracted from $s(X, Z)$.

Those target points, which can be reconstructed from the different antenna locations, have multiple normal vectors as \mathbf{e}_n related to the second scattering directions \mathbf{e}_3 as described in the proposed method. Consequently, even in the case that the first scattering points exist on an edge, i.e., $s(X, Z)$ includes an edge diffraction, this method selects the optimum first scattering point $\hat{\mathbf{p}}_1$ in (19) and sequentially determines $\hat{\mathbf{p}}_2$ for each (X, Z_D) . Also, while Z_D possibly includes no double scattered range points accidentally extracted from range sidelobes of single scattered signals, or other scattering components, this figure validates the fact that the false image reduction postprocessing successfully eliminates these false points. Besides, it has a great advantage in computation time, which requires less than 0.4 s for Intel Pentium D 2.8-GHz processor with 800 MB effective memory. As previously mentioned in Section II-B2, the conventional method costs around 60 s, and it is distinctly improved as to the computation burden. However, some fluctuations of the estimated points occur around the rectangular side, regardless of a noiseless situation. This is because the method employs the range derivative in (9), which tends to enhance small errors caused by the scattered waveform deformations or other interference effects.

For another target case, a deep-set concave boundary is investigated. Fig. 9 shows the target points estimated by RPM and the proposed method, respectively, where the true range points are given. It is confirmed that our method successfully enhances the imaging range around the side of the concave boundary, using the double scattered range points. Fig. 10 shows the output of a

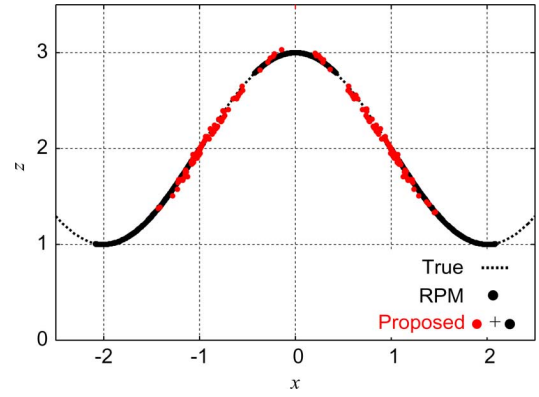


Fig. 9. Estimated image with RPM and the proposed method for the concave target, when true range points are given.

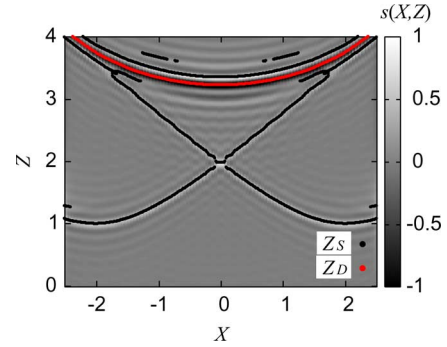


Fig. 10. Output of Wiener filter $s(X, Z)$ for the concave target and range points as (X, Z_S) and (X, Z_D) .

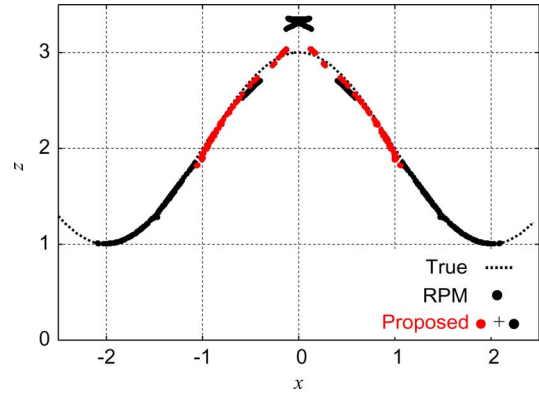


Fig. 11. Estimated image with RPM and the proposed method for the concave targets, when range points are extracted from $s(X, Z)$.

Wiener filter, which is calculated by FDTD, and each extracted range point as (X, Z_S) and (X, Z_D) . Fig. 11 presents the estimated image created by the proposed method. It verifies that, in the practical case, it can produce accurate target points around the side of the concave boundary, which are not seen for RPM. The calculation time is also around 0.4 s with the same processor previously described, which is definitely improved from that required by the conventional method around 60 s.

Here, the quantitative analysis is introduced by ϵ_i defined as

$$\epsilon_i = \min_{\mathbf{p}_{\text{true}}} \|\mathbf{p}_{\text{true}} - \mathbf{p}_e^i\|, \quad (i = 1, 2, \dots, N_T) \quad (25)$$

where \mathbf{p}_{true} and \mathbf{p}_e^i express the locations of the true and estimated target points, respectively. N_T is the total number of \mathbf{p}_e^i . Fig. 12 plots the number of estimated points for each value of

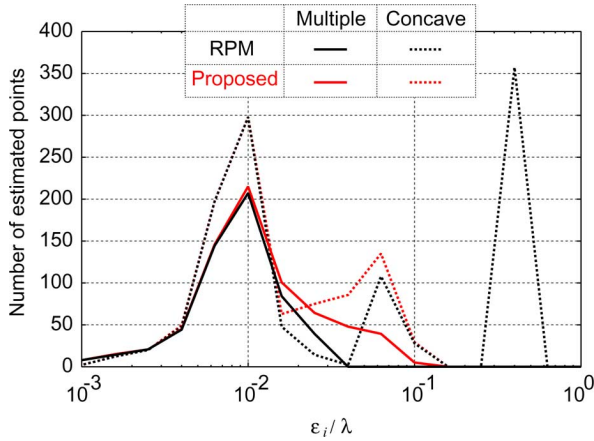


Fig. 12. Number of target points for each ϵ_i , in the case of Figs. 8 and 11.

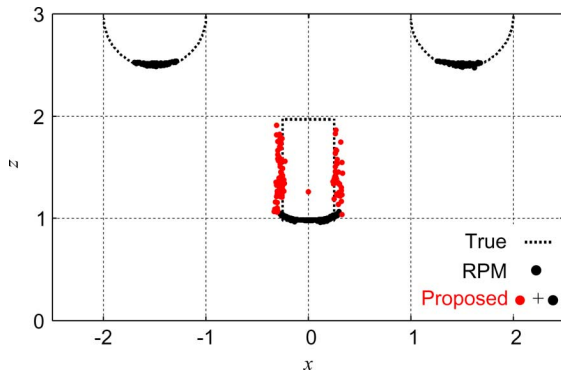


Fig. 13. Estimated image with RPM and the proposed method for the multiple targets at SN = 30 dB.

ϵ in both cases as Figs. 8 and 11. It verifies that the number of accurate target points with the proposed method significantly increases around 0.03λ , simultaneously enhancing the imaging range. The mean value of ϵ_i as $\bar{\epsilon}$ is $1.25 \times 10^{-2}\lambda$ for the multiple objects, and this result quantitatively proves the effectiveness of the proposed method as to accurate imaging. In the case of the concave boundary, $\bar{\epsilon}$ becomes $1.06 \times 10^{-1}\lambda$, because there are many false image points over the actual boundary as in Fig. 11 for both RPM and the proposed method. This inaccuracy is mainly contributed by the conventional RPM, not by the proposed method. The reason for this is that more than a triple scattering effect produces an unnecessary image.

Furthermore, an example in noisy situation is investigated, whereby white Gaussian noise is added to each received signal as $s'(X, Z)$. Fig. 13 shows the estimated points obtained by the proposed method, where the mean S/N is 30 dB. S/N is defined as the ratio of peak instantaneous signal power to the average noise power after applying the matched filter with the transmitted waveform. Although the accuracy of the estimated target points deteriorates due to the false range points extracted from noisy components, the whole image can offer a significant target boundary including the side of the rectangular boundary. Also, it should be noted that the range fluctuations caused by noise are effectively suppressed by the Gaussian weighted difference approach in (24) using an appropriate σ_{DX} .

Next, the relationship between $\bar{\epsilon}$ and S/N is investigated for multiple objects as in Fig. 14 for each σ_{DX} . The figure shows that the proposed method obtains a sufficient accuracy less than

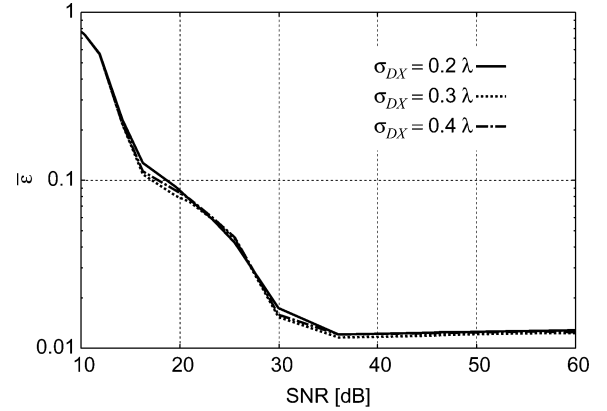


Fig. 14. Relationship between $\bar{\epsilon}$ and S/N for each σ_{DX} as to the multiple objects.

0.02λ over SN ≥ 30 dB using any value of σ_{DX} . While this method requires an apparently high S/N to hold the accuracy, the definition of S/N used in this paper overestimates the practical S/N because it considers not only a frequency localization of the received pulse but also a temporal one. Indeed, the actual UWB radar system can achieve this level of S/N, because we assume a near field measurement, where each receiver obtains an intensive echo from objects even under the spectrum mask of the UWB signal [19], and random noises in received signals can be considerably suppressed using coherent averaging.

Moreover, to consider the applicability of the method to a realistic scenario, the sensitivity of antenna location to inaccuracy is investigated. This is mainly caused by mechanical errors in the scanning system. Figs. 15 and 16 show the output of Wiener filter with extracted range points and the estimated image with RPM and the proposed method at SN = 30 dB, respectively. The spatial errors with the Gaussian distribution are added to each antenna location $(X, 0)$ in calculating the received signals. The standard deviation of the errors is set to 0.01λ , which corresponds to 1-mm accuracy for the antenna positioning, in the case of 100-mm center wavelength of the UWB pulse. This can be obtained by the real scanning systems used in [14]. The figure shows that the proposed method still creates an accurate image including the shadow region; $\bar{\epsilon}$ denotes $1.51 \times 10^{-2}\lambda$ in this case. The first reason for this is that RPM has a significant tolerance to random noise or system errors because it employs the global characteristic of the range points distribution; there is only a slight image degradation as shown in the figure. The second reason is that the proposed method employs the smoothing scheme in calculating the range derivative in (24), and the false image reduction as postprocessing, in order to avoid image distortions from system errors or receiver noise and enhance the credibility of the obtained images.

Finally, the limitation of this method is discussed as follows. The proposed method, which does have some limitations, has two main requirements: a scanning orbit and a clear boundary assumption for objects. First, while this paper assumes linear antenna scanning, it can be extended to arbitrary curvilinear scanning by modifying (7). However, the scanning line must be differentiable because the method employs derivative operation along it. Second, although the method assumes a clear boundary for objects, in the case of a human body, this assumption is

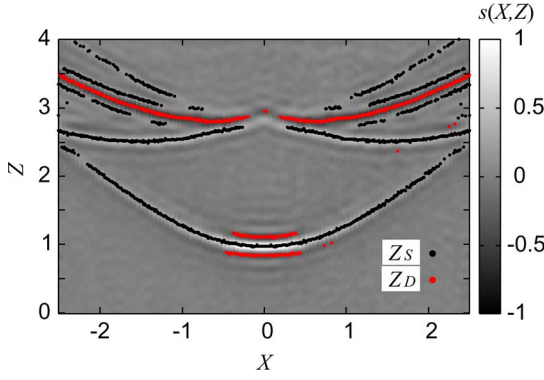


Fig. 15. Output of Wiener filter and extracted range points for the multiple targets, where random errors are given to antenna locations $(X, 0)$.

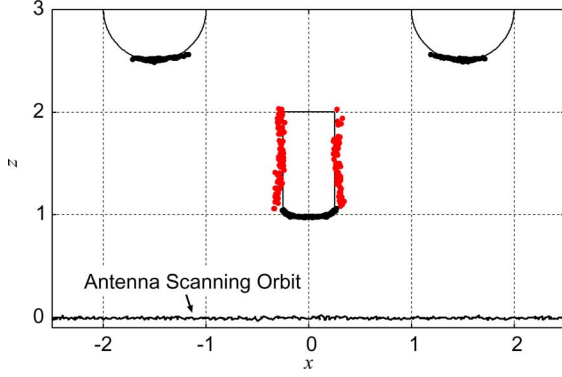


Fig. 16. Estimated image with RPM and the proposed method for the multiple targets where random errors are given to antenna locations $(X, 0)$.

hardly acceptable, and then, both the conventional and the proposed methods offer blurry images expressing statistical scattering centers. On the other hand, with respect to a UWB waveform, any waveform holding the same equivalent bandwidth with lower a range sidelobe is applicable to this method, for example, a pulse, chirping signal, or spread spectrum (M-sequence) waveforms. This is because the proposed method uses only the significant ranges, which can be extracted from the local maxima or minima of the output of Wiener filter using any possible transmitted waveform with enough S/N level. Consequently, the performance limitation depends mainly on the bandwidth of the transmitted pulse and the S/N level. In addition, while this paper assumes mono-static observation, it is easily extended to a bi-static model, required for a realistic radar constitution, employing the same approach in the proposed method. This is our future task.

III. 3-D PROBLEM

A. System Model

Fig. 17 shows a system model for the 3-D problem. The target model, antenna, and transmitted signal are the same as those assumed for the 2-D problem. The antenna is scanned on the plane, $z = 0$. It assumes a linear polarization in the direction of the x -axis. A spherical wave propagation is assumed. R-space is expressed by the parameter (x, y, z) . We assume $z \geq 0$ for simplicity. $s'(X, Y, Z)$ is defined as the received electric field at the antenna location $(x, y, z) = (X, Y, 0)$. $s(X, Y, Z)$ is defined

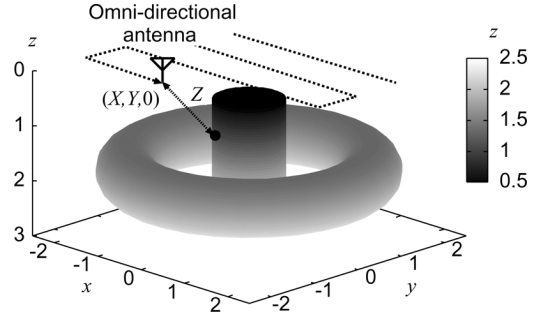


Fig. 17. System model in 3-D problem.

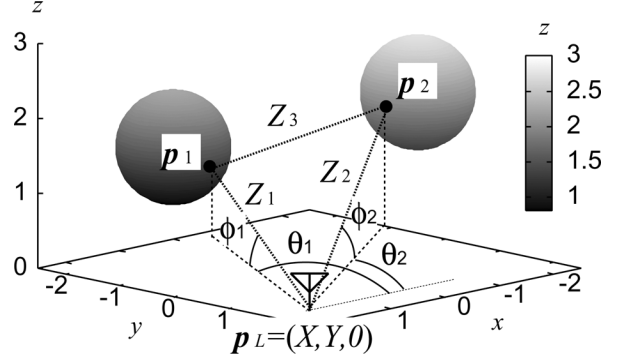


Fig. 18. Relationship among \mathbf{p}_1 , \mathbf{p}_2 and \mathbf{p}_L in 3-D model.

as the output of the Wiener filter with the transmitted waveform. As similar to the 2-D case, The two sets of range points are extracted from the local maxima and minima as (X, Y, Z_S) and (X, Y, Z_D) , respectively.

B. Proposed Method for the 3-D Problem

This section describes the 3-D model of the proposed method. Here, an antenna location is redefined as $\mathbf{p}_L = (X, Y, 0)$. The first scattering point as \mathbf{p}_1 and the second one as \mathbf{p}_2 are also redefined as

$$\mathbf{p}_i \equiv (x_i, y_i, z_i) = \mathbf{p}_L + \begin{bmatrix} Z_i \cos \theta_i \cos \phi_i \\ Z_i \sin \theta_i \cos \phi_i \\ Z_i \sin \phi_i \end{bmatrix}^T, \quad (i = 1, 2) \quad (26)$$

where $0 \leq \theta_1, \theta_2 < 2\pi$ and $0 < \phi_1, \phi_2 \leq \pi/2$ hold. Fig. 18 shows the relationship among \mathbf{p}_1 , \mathbf{p}_2 , and \mathbf{p}_L in the 3-D model. Similar to the 2-D model, the following proposition holds.

Proposition 2: If $\partial Z_D / \partial X$ and $\partial Z_D / \partial Y$ exist on each range point (X, Y, Z_D) , the next formulations hold:

$$\left. \begin{aligned} \frac{\partial Z_D}{\partial X} &= \frac{\cos \theta_1 \cos \phi_1 + \cos \theta_2 \cos \phi_2}{2} \\ \frac{\partial Z_D}{\partial Y} &= \frac{\sin \theta_1 \cos \phi_1 + \sin \theta_2 \cos \phi_2}{2} \end{aligned} \right\}. \quad (27)$$

The derivation of this proposition is described in Appendix C. Once \mathbf{p}_1 is determined, ϕ_2 and θ_2 can be calculated as

$$\begin{aligned} \phi_2 &= \cos^{-1} \left\{ \sqrt{(2\partial Z_D / \partial X + \cos \theta_1 \cos \phi_1)^2} \right. \\ &\quad \left. + \sqrt{(2\partial Z_D / \partial Y + \sin \theta_1 \cos \phi_1)^2} \right\} \\ \theta_2 &= \arg \left\{ \left(\frac{2\partial Z_D / \partial X - \cos \theta_1 \cos \phi_1}{\cos \phi_2} \right) \right\} \end{aligned} \quad (28)$$

$$+j \left(\frac{2\partial Z_D/\partial Y - \sin \theta_1 \cos \phi_1}{\cos \phi_2} \right) \} \quad (29)$$

where j denotes an imaginary unit.

In this extension, target points redefined as $\mathbf{p}_i^{\text{rpm}} \equiv (x_i^{\text{rpm}}, y_i^{\text{rpm}}, z_i^{\text{rpm}})$ corresponding to the range points as $\mathbf{q}_i \equiv (X_i^{\text{rpm}}, Y_i^{\text{rpm}}, Z_i^{\text{rpm}})$, ($i = 1, \dots, N_R^{\text{rpm}}$) obtained by RPM are employed [13]. Each normal vector $\mathbf{e}_{n,i}^{\text{rpm}}$ is also calculated as

$$\mathbf{e}_{n,i}^{\text{rpm}} = \frac{(X_i^{\text{rpm}} - x_i^{\text{rpm}}, Y_i^{\text{rpm}} - y_i^{\text{rpm}}, -z_i^{\text{rpm}})}{Z_i^{\text{rpm}}}. \quad (30)$$

And then, the parameter vector \mathbf{P}_i defined in (14) is constituted by redefining $\mathbf{Q}_D \equiv (\mathbf{p}_L, Z_D, \partial Z_D/\partial X, \partial Z_D/\partial Y)$, and updating $\mathbf{e}_{3,i}^{\text{rpm}}$ in (11).

Using the above parameters, the target points in the 3-D model are basically calculated according to the procedure of the proposed method in the 2-D case, as in Section II-C3. Some modifications for the procedure are described below. As in Step 2), the range point $(X, Y, Z_{D,i})$ is extracted from the output of a Wiener filter $s(X, Y, Z)$, where the following condition satisfies:

$$\left. \begin{aligned} \partial s(X, Y, Z)/\partial Z &= 0 \\ s(X, Y, Z) &\leq \beta \min_Z s(X, Y, Z) \end{aligned} \right\} \quad (31)$$

Also, in Step 3), $\partial Z_{D,j}/\partial Y$ is calculated as

$$\frac{\partial Z_{D,j}}{\partial Y} = \frac{\sum_{k=1}^{N'_D} \frac{Z_{D,j} - Z_{D,k}}{Y_j - Y_k} \exp \left\{ -\frac{(Y_j - Y_k)^2}{2\sigma_{DY}^2} \right\}}{\sum_{k=1}^{N'_D} \exp \left\{ -\frac{(Y_j - Y_k)^2}{2\sigma_{DY}^2} \right\}} \quad (32)$$

where $\sigma_{DY} = \sigma_{DX}$, and N'_D denotes the number of the range points which satisfy $|(Z_{D,j} - Z_{D,k})/(Y_j - Y_k)| \leq 1$ around $(X, Y_j, Z_{D,j})$.

C. Performance Evaluation Using Numerical Simulation

This section presents two examples of the proposed method with different target cases, using a numerical simulation. The mono-static radar is scanned for $-2.5 \leq x, y \leq 2.5$, where the number of locations on each axis is 101. Here, $\sigma_{DX} = \sigma_{DY} = 0.3\lambda$, $\beta = 0.3$ and $\gamma = 100$ are set. First, the target boundary is assumed as in Fig. 17. Fig. 19 illustrates the estimated target points obtained by RPM and the proposed method, where the true range points are given by the geometrical optics approximation, similar to 2-D case. This figure verifies that the imaging points express a quite accurate target boundary including the side of the cylindrical objects. This is because the double scattered wave propagates along the side of the toric and cylindrical boundaries. Next, Fig. 20 shows the range points as (X, Y, Z_S) and (X, Y, Z_D) extracted from the output of a Wiener filter, which is calculated by FDTD. Figs. 21 and 22 depict the estimated 3-D image and its cross-section at $-0.1 \leq x \leq 0.1$, respectively. These figures show that the obtained image of the proposed method, in this case, accurately creates the side of the cylindrical boundary, which cannot be reconstructed by RPM.

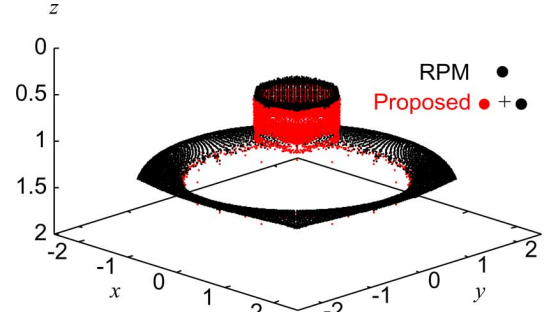


Fig. 19. Estimated 3-D image with RPM and the proposed method for the targets as in Fig. 17, when true range points are given.

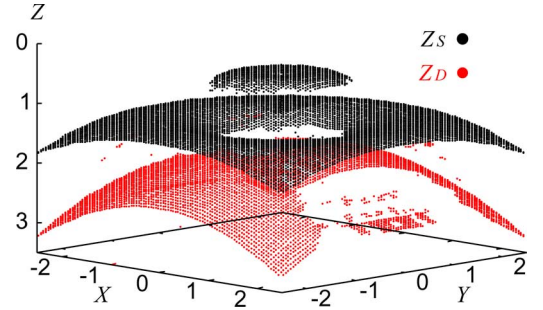


Fig. 20. Extracted range points of single and double scattered waves for the targets in Fig. 17.

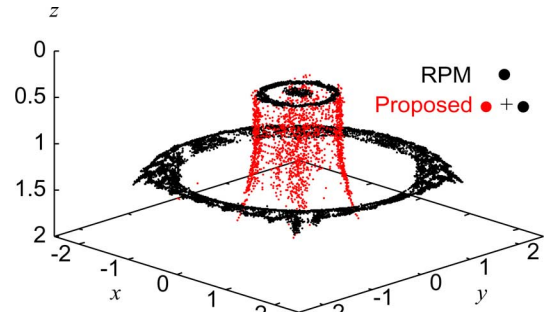


Fig. 21. Estimated 3-D image with RPM and the proposed method for the targets as in Fig. 17, when range points are extracted from $s(X, Y, Z)$.

There are some divergent images around the target side, which are basically caused by the errors of range derivatives. This method creates the target points, not the intensified SAR image, which contributes to the identification of the edge or wedge region. Note that, the proposed method requires only 10 s for a full 3-D image after creating the target points with RPM. This amount is prominently reduced from that of the conventional method based on the fifth times integral for imaging after SAR processing [15], requiring around 10^6 s.

For another example, a concave target is shown in Fig. 23. Fig. 24 offers the estimated 3-D boundary performed by the proposed method, where the true range points are given. This verifies that the proposed method accomplishes an accurate target imaging including the side of the concave boundary. Fig. 25 shows the extracted range points from the output of a Wiener filter. Figs. 26 and 27 present the 3-D target image and its cross section at $-0.1 \leq x \leq 0.1$, respectively, where the received data is calculated by FDTD. This figure also proves that the proposed method creates an accurate image around the deep side of

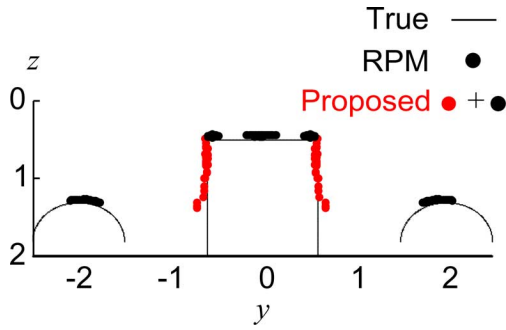


Fig. 22. Cross-section image of Fig. 21 for $-0.1 \leq x \leq 0.1$.

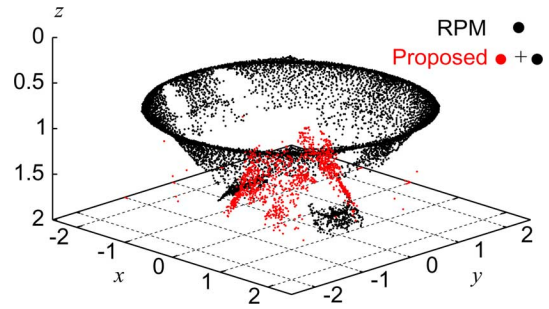


Fig. 26. Estimated 3-D image with RPM and the proposed method for the targets in Fig. 23, when range points are extracted from $s(X, Y, Z)$.

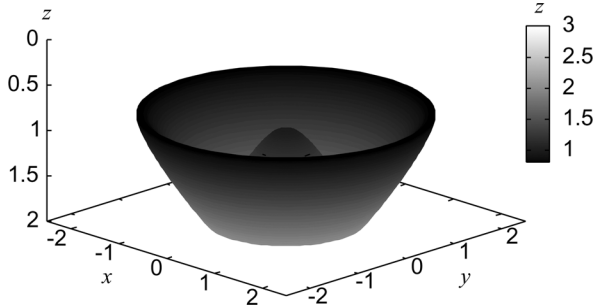


Fig. 23. True concave target boundary.

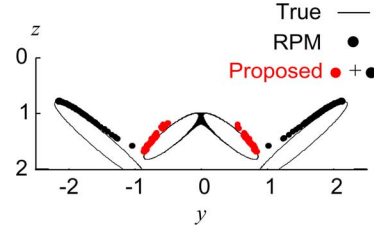


Fig. 27. Cross-section image of Fig. 26 for $-0.1 \leq x \leq 0.1$.

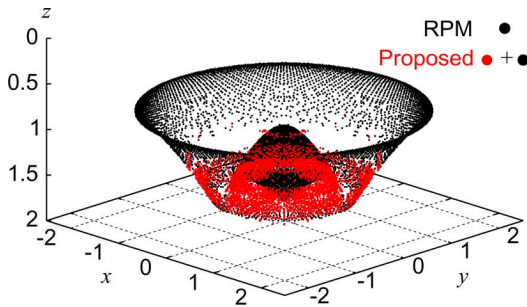


Fig. 24. Estimated 3-D image with RPM and the proposed method for the targets in Fig. 23, when true range points are given.

	Torus+Cylinder	Concave
RPM	—
Proposed	—

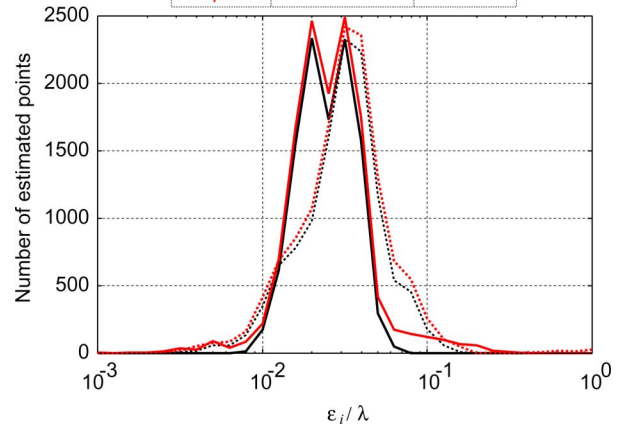


Fig. 28. Number of target points for each ϵ_i in the case of Figs. 21 and 26.

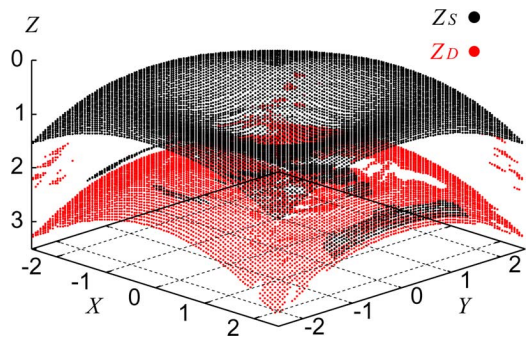


Fig. 25. Extracted range points of single (black) and double (red) scattered waves for targets in Fig. 23.

the concave boundary, which is focused by the double scattered signal.

Furthermore, a quantitative analysis for these examples is presented as follows. Fig. 28 shows the number of target points for each accuracy ϵ_i , that is defined as in (25) for the target cases as in Figs. 21 and 26. This figure shows that the proposed method increases accurate target points around 0.03λ and avoids the accuracy distortion for both target cases. The mean value of

this error index as $\bar{\epsilon}$ is 0.028λ for the toric and cylindrical targets, and 0.059λ for the deep-set concave targets, respectively. This quantitatively shows that the proposed method enhances the imaging range even in the 3-D model, accomplishing much faster image processing.

In addition, an example of a noisy situation is presented. White Gaussian noise is added to the received signal $s(X, Y, Z)$. Fig. 29 shows the estimated target boundaries of the RPM and the proposed method, with S/N around 30 dB. This figure shows that, while the proposed method suffers from image fluctuations caused by random noise, it still offers a significant image expansion around the side of the torus boundary. $\bar{\epsilon} = 3.02 \times 10^{-2}\lambda$ in this case.

Finally, the computational complexities of the algorithms are compared. The conventional SAR based method requires around $\mathcal{O}(N_X N_Y N_x^2 N_y^2 N_z^2)$, where $N_X, N_Y, N_x, N_y,$ and N_z denote the sampling numbers for the antenna location $X, Y,$ and the spatial coordinates x, y and z , respectively, and $\mathcal{O}(\ast)$ gives the Landau notation. This is because the conventional

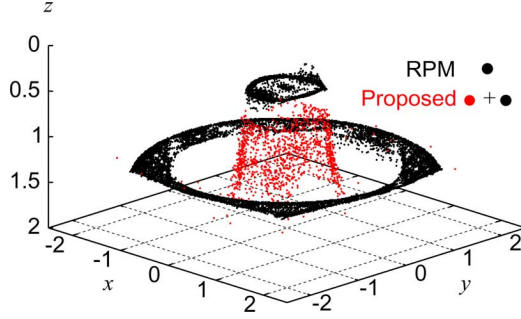


Fig. 29. Estimated 3-D image with RPM and the proposed method for the targets in Fig. 17 at SN = 30 dB.

TABLE I
CALCULATION TIME (FOR INTEL PENTIUM D 2.8 GHz PROCESSOR) AND
COMPUTER COMPLEXITY OF EACH ALGORITHM

	Calculation time	Computational complexity
Conventional	Around 10^6 sec	$\mathcal{O}(N_X N_Y N_x^2 N_y^2 N_z^2)$
Proposed	10 sec	$\mathcal{O}(N_X^2 N_Y^2)$

SAR-based method should employ a quintuple integration for each image voxel as in [15]. On the contrary, the proposed method requires around $\mathcal{O}(N_X^2 N_Y^2)$, since it requires only a searching operation to the first scattering points obtained by RPM ($\mathcal{O}(N_X N_Y)$) for each range point ($\mathcal{O}(N_X N_Y)$). Table I shows a comparison for computational times using an Intel Pentium D 2.8-GHz processor with 800-MB memory, and the computational complexity for each method. In this case, $N_X = N_Y = 101$, $N_x = N_y = 101$, and $N_z = 51$, where each voxel size is 0.05λ . This table shows that the computation required for the proposed method is reduced to 10^5 times that of the conventional method. Moreover, even if the fast processing of the SAR like omega-k migration [18] were to be adopted to double scattering aperture synthesis, it would have an essential problem that the computation complexity severely depends, in principle, on the voxel size or imaging range. On the contrary, the proposed method, based on range points migration, is quite different from SAR, and it does not need to determine the voxel size or imaging region, owing to the mapping from the observed range points to the target boundary points. The computation required depends only on the number of observed range points, which is on the order of the square of the antenna scanning samples.

IV. CONCLUSION

This paper proposed a novel imaging algorithm for expanding the imaging range, which efficiently utilizes the range derivative of double scattered waves. The proposed method elicits some inherent characteristics in the RPM method and achieves direct shadow imaging without using any integration process. This method has an outstanding advantage that it accomplishes extremely high-speed imaging by specifying a clear boundary extraction, simultaneously extending the visible region without *a priori* knowledge of target or surroundings. It has the additional advantage that the target boundary can be expressed as a group of target points, which enables the identification of an edge or

wedge region and helps to classify the target structure. Numerical simulations in the 2-D and 3-D models, including multiple objects and concave shaped objects showed that the proposed method substantially extended the imaging range with extremely high speed, even if the model errors and random noises are added to the received data. This exemplifies a significant applicability to the realistic radar sensing scenario. Particularly for the 3-D problem, it is a more than 10^5 times improvement compared with that of the conventional SAR-based method as to the computational complexity. Consequently, this method can significantly contribute to the design of real-time sensors, as found in robots or security systems.

APPENDIX A DERIVATION OF (7)

$\partial Z_D / \partial X$ is divided into three terms as

$$\frac{\partial Z_D}{\partial X} = \frac{1}{2} \left(\frac{\partial Z_1}{\partial X} + \frac{\partial Z_2}{\partial X} + \frac{\partial Z_3}{\partial X} \right). \quad (33)$$

Here, Z_D is expressed as

$$Z_D = \frac{Z_1 + Z_2 + Z_3}{2} \quad (34)$$

where $Z_1 = \sqrt{(x_1 - X)^2 + z_1^2}$, $Z_2 = \sqrt{(x_2 - X)^2 + z_2^2}$, $Z_3 = \sqrt{(x_1 - x_2)^2 + (z_1 - z_2)^2}$ hold. Each partial derivative of X is given as

$$\frac{\partial Z_1}{\partial X} = -\frac{x_1 - X}{Z_1} + \mathbf{e}_1 \cdot \frac{\partial \mathbf{p}_1}{\partial X} \quad (35)$$

$$\frac{\partial Z_2}{\partial X} = -\frac{x_2 - X}{Z_2} + \mathbf{e}_2 \cdot \frac{\partial \mathbf{p}_2}{\partial X} \quad (36)$$

$$\frac{\partial Z_3}{\partial X} = \mathbf{e}_3 \cdot \left(\frac{\partial \mathbf{p}_2}{\partial X} - \frac{\partial \mathbf{p}_1}{\partial X} \right) \quad (37)$$

where

$$\mathbf{e}_1 = \left(\frac{x_1 - X}{Z_1}, \frac{z_1}{Z_1} \right) \quad (38)$$

$$\mathbf{e}_2 = \left(\frac{x_2 - X}{Z_2}, \frac{z_2}{Z_2} \right) \quad (39)$$

$$\mathbf{e}_3 = \left(\frac{x_2 - x_1}{Z_3}, \frac{z_2 - z_1}{Z_3} \right) \quad (40)$$

$$\frac{\partial \mathbf{p}_1}{\partial X} \equiv \left(\frac{\partial x_1}{\partial X}, \frac{\partial z_1}{\partial X} \right) = \frac{\partial x_1}{\partial X} \left(1, \frac{\partial z_1}{\partial x_1} \right) \quad (41)$$

$$\frac{\partial \mathbf{p}_2}{\partial X} \equiv \left(\frac{\partial x_2}{\partial X}, \frac{\partial z_2}{\partial X} \right) = \frac{\partial x_2}{\partial X} \left(1, \frac{\partial z_2}{\partial x_2} \right) \quad (42)$$

hold. In this case, we assume that the reflection path of the double scattered path satisfies the law of reflection and the following relationships hold:

$$\frac{\partial \mathbf{p}_1}{\partial X} \cdot (\mathbf{e}_1 - \mathbf{e}_3) = 0 \quad (43)$$

$$\frac{\partial \mathbf{p}_2}{\partial X} \cdot (\mathbf{e}_2 + \mathbf{e}_3) = 0. \quad (44)$$

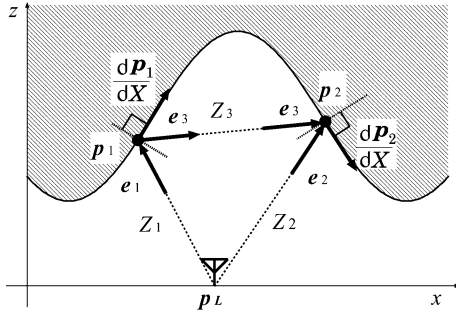


Fig. 30. Relationship among e_1 , e_2 , $e_2 \partial \mathbf{p}_1 / \partial X$, and $\partial \mathbf{p}_2 / \partial X$.

Fig. 30 shows the relationship among those parameters. Substituting these equations to (35)–(37), (7) is obtained.

APPENDIX B DERIVATION OF (10)

Using \mathbf{p}_1 , e_3 , Z_1 , Z_2 , and Z_D defined in Section II-C, \mathbf{p}_2 is expressed as

$$\mathbf{p}_2 = \mathbf{p}_1 + (2Z_D - Z_1 - Z_2) \mathbf{e}_3. \quad (45)$$

Obviously, the next equation holds from the definition of Z_2 :

$$Z_2 = \|\mathbf{p}_2 - \mathbf{p}_L\| = \|\mathbf{p}_1 - \mathbf{p}_L + (2Z_D - Z_1 - Z_2) \mathbf{e}_3\|. \quad (46)$$

Squaring the both side of (46) and rearranging as to Z_2 , (10) is obtained. This relationship obviously holds in 3-D problem.

APPENDIX C DERIVATION OF (27)

We introduce the partial derivatives of Z_D for the two directions along X and Y axis as

$$\frac{\partial Z_D}{\partial X} = \frac{1}{2} \left(\frac{\partial Z_1}{\partial X} + \frac{\partial Z_2}{\partial X} + \frac{\partial Z_3}{\partial X} \right) \quad (47)$$

$$\frac{\partial Z_D}{\partial Y} = \frac{1}{2} \left(\frac{\partial Z_1}{\partial Y} + \frac{\partial Z_2}{\partial Y} + \frac{\partial Z_3}{\partial Y} \right) \quad (48)$$

where $Z_D = (Z_1 + Z_2 + Z_3)/2$, $Z_1 = \sqrt{(x_1 - X)^2 + (y_1 - Y)^2 + z_1^2}$, $Z_2 = \sqrt{(x_2 - X)^2 + (y_2 - Y)^2 + z_2^2}$, and $Z_3 = \sqrt{(x_1 - x_2)^2 + (y_1 - y_2)^2 + (z_1 - z_2)^2}$ hold. In the similar to the 2-D case in (35)–(37), the following equation as to $\partial Z_D / \partial Y$ holds:

$$\frac{\partial Z_1}{\partial Y} = -\frac{y_1 - Y}{Z_1} + \mathbf{e}_1 \cdot \frac{\partial \mathbf{p}_1}{\partial Y} \quad (49)$$

$$\frac{\partial Z_2}{\partial Y} = -\frac{y_2 - Y}{Z_2} + \mathbf{e}_2 \cdot \frac{\partial \mathbf{p}_2}{\partial Y} \quad (50)$$

$$\frac{\partial Z_3}{\partial Y} = \mathbf{e}_3 \cdot \left(\frac{\partial \mathbf{p}_2}{\partial Y} - \frac{\partial \mathbf{p}_1}{\partial Y} \right) \quad (51)$$

where $\partial X / \partial Y = 0$ is used, and

$$\mathbf{e}_1 = \left(\frac{x_1 - X}{Z_1}, \frac{y_1 - Y}{Z_1}, \frac{z_1}{Z_1} \right) \quad (52)$$

$$\mathbf{e}_2 = \left(\frac{x_2 - X}{Z_2}, \frac{y_2 - Y}{Z_2}, \frac{z_2}{Z_2} \right) \quad (53)$$

$$\mathbf{e}_3 = \left(\frac{x_2 - x_1}{Z_3}, \frac{y_2 - y_1}{Z_3}, \frac{z_2 - z_1}{Z_3} \right) \quad (54)$$

$$\frac{\partial \mathbf{p}_1}{\partial Y} \equiv \left(\frac{\partial x_1}{\partial Y}, \frac{\partial y_1}{\partial Y}, \frac{\partial z_1}{\partial Y} \right) = \frac{\partial x_1}{\partial Y} \left(1, 0, \frac{\partial z_1}{\partial x_1} \right) \quad (55)$$

$$\frac{\partial \mathbf{p}_2}{\partial Y} \equiv \left(\frac{\partial x_2}{\partial Y}, \frac{\partial y_2}{\partial Y}, \frac{\partial z_2}{\partial Y} \right) = \frac{\partial x_2}{\partial Y} \left(1, 0, \frac{\partial z_2}{\partial x_2} \right) \quad (56)$$

hold, where $\partial y_1 / \partial x_1 = 0$ and $\partial y_2 / \partial x_2 = 0$ are used. Then, the similar relationships hold as

$$\frac{\partial \mathbf{p}_1}{\partial Y} \cdot (\mathbf{e}_1 - \mathbf{e}_3) = 0 \quad (57)$$

$$\frac{\partial \mathbf{p}_2}{\partial Y} \cdot (\mathbf{e}_2 + \mathbf{e}_3) = 0. \quad (58)$$

Substituting them to (49)–(51), (27) as to $\partial Z_D / \partial Y$ is derived. Using the same approach, (27) for $\partial Z_D / \partial X$ is obtained.

REFERENCES

- [1] T. C. Williams, J. M. Sill, and E. C. Fear, "Breast surface estimation for radar-based breast imaging system," *IEEE Trans. Biomed. Eng.*, vol. 55, no. 6, pp. 1678–1686, Jun. 2008.
- [2] D. W. Winters, J. D. Shea, E. L. Madsen, G. R. Frank, B. D. Van Veen, and S. C. Hagness, "Estimating the breast surface using UWB microwave monostatic backscatterer measurements," *IEEE Trans. Biomed. Eng.*, vol. 55, no. 1, pp. 247–256, Jan. 2008.
- [3] D. L. Mensa, G. Heidbreder, and G. Wade, "Aperture synthesis by object rotation in coherent imaging," *IEEE Trans. Nucl. Sci.*, vol. NS-27, no. 2, pp. 989–998, Apr. 1980.
- [4] D. Liu, G. Kang, L. Li, Y. Chen, S. Vasudevan, W. Joines, Q. H. Liu, J. Krolik, and L. Carin, "Electromagnetic time-reversal imaging of a target in a cluttered environment," *IEEE Trans. Antenna Propag.*, vol. 53, no. 9, pp. 3058–3066, Sep. 2005.
- [5] D. Liu, J. Krolik, and L. Carin, "Electromagnetic target detection in uncertain media: Time-reversal and minimum-variance algorithms," *IEEE Trans. Geosci. Remote Sens.*, vol. 45, no. 4, pp. 934–944, Apr. 2007.
- [6] J. Song, Q. H. Liu, P. Torrione, and L. Collins, "Two-dimensional and three dimensional NUFFT migration method for landmine detection using ground-penetrating radar," *IEEE Trans. Geosci. Remote Sens.*, vol. 44, no. 6, pp. 1462–1469, Jun. 2006.
- [7] F. Soldovieri, A. Brancaccio, G. Prisco, G. Leone, and R. Pieri, "A Kirchhoff-based shape reconstruction algorithm for the multimostatic configuration: The realistic case of buried pipes," *IEEE Trans. Geosci. Remote Sens.*, vol. 46, no. 10, pp. 3031–3038, Oct. 2008.
- [8] A. Massa, D. Franceschini, G. Franceschini, M. Pastorino, M. Raffetto, and M. Donelli, "Parallel GA-based approach for microwave imaging applications," *IEEE Trans. Antenna Propag.*, vol. 53, no. 10, pp. 3118–3127, Oct. 2005.
- [9] T. Sakamoto and T. Sato, "A target shape estimation algorithm for pulse radar systems based on boundary scattering transform," *IEICE Trans. Commun.*, vol. E87-B, no. 5, pp. 1357–1365, 2004.
- [10] S. Kidera, T. Sakamoto, and T. Sato, "High-resolution and real-time UWB radar imaging algorithm with direct waveform compensations," *IEEE Trans. Geosci. Remote Sens.*, vol. 46, no. 11, pp. 3503–3513, Nov. 2008.
- [11] S. Hantscher, A. Reizenzahn, and C. G. Diskus, "Through-wall imaging with a 3-D UWB SAR algorithm," *IEEE Signal Process. Lett.*, vol. 15, no. 2, pp. 269–272, Feb. 2008.
- [12] H. Wang, H. Xue, and M. Ge, "Application and practice of system integration approach in intelligent human motion recognition," in *Proc. Int. Conf. Comput. Sci. Software Eng.*, 2008, vol. 1.
- [13] S. Kidera, T. Sakamoto, and T. Sato, "Accurate UWB radar 3-D imaging algorithm for complex boundary without range points connections," *IEEE Trans. Geosci. Remote Sens.*, vol. 48, no. 4, pp. 1993–2004, Apr. 2010.
- [14] S. Kidera, T. Sakamoto, and T. Sato, "Super-resolution UWB radar imaging algorithm based on extended capon with reference signal optimization," *IEEE Trans. Antenna Propag.*, vol. 59, no. 5, pp. 1606–1615, May 2011.

- [15] S. Kidera, T. Sakamoto, and T. Sato, "Experimental study of shadow region imaging algorithm with multiple scattered waves for UWB radars," in *Proc. PIERS'09*, Aug. 2009, vol. 5, no. 4, pp. 393–396.
- [16] J. M. F. Moura and Y. Jin, "Detection by time reversal: Single antenna," *IEEE Trans. Signal Process.*, vol. 55, no. 1, pp. 187–201, Jan. 2007.
- [17] G. Shi and A. Nehorai, "Cramer–Rao bound analysis on multiple scattering in multistatic point-scatterer estimation," *IEEE Trans. Signal Process.*, vol. 55, no. 6, pp. 2840–2850, Jun. 2007.
- [18] X. Xu, E. L. Miller, and C. M. Rappaport, "Minimum entropy regularization in frequency-wavenumber migration to localize subsurface objects," *IEEE Trans. Geosci. Remote Sens.*, vol. 41, no. 8, pp. 1804–1812, Aug. 2003.
- [19] Federal Communications Commission (FCC), Office of Engineering and Technology (OET) Bulletin No. 65, Supplement C, Aug. 1997, p. 35.



Shouhei Kidera (M'11) received the B.E. degree in electrical and electronic engineering from Kyoto University, Kyoto, Japan, in 2003 and M.I. and Ph.D. degrees in informatics from Kyoto University in 2005 and 2007, respectively.

He is an Assistant Professor in the Graduate School of Informatics and Engineering, University of Electro-Communications, Tokyo, Japan. His current research interest is in advanced signal processing for the near field radar, UWB radar.

Prof. Kidera is a member of the Institute of Electronics, Information, and Communication Engineers of Japan (IEICE) and the Institute of Electrical Engineering of Japan (IEEJ).



Tetsuo Kirimoto (M'91–SM'97) received the B.S., M.S., and Ph.D. degrees in communication engineering from Osaka University, Osaka, Japan, in 1976, 1978, and 1995, respectively.

From 1978 to 2003, he was with Mitsubishi Electric Corp. studying radar signal processing. From 1982 to 1983, he was a Visiting Scientist at the Remote Sensing Laboratory, University of Kansas. From 2003 to 2007, he was with the University of Kitakyushu as a Professor. Since 2007, he has been with the University of Electro-Communications, Tokyo, Japan, where he is a Professor at the Graduate School of Informatics and Engineering. His current study interests include digital signal processing and its application to various sensor systems.

Prof. Kirimoto is a member of the Institute of Electronics, Information, and Communication Engineers (IEICE) and the Society of Instrument and Control Engineering (SICE) of Japan.